

Magnetorotational instability driven dynamos at low magnetic Prandtl numbers

P. J. Käpylä^{1,2} and M. J. Korpi¹

¹*Department of Physics, Gustaf Hällströmin katu 2a (PO Box 64), FI-00064 University of Helsinki, Finland*

²*NORDITA, AlbaNova University Center, Roslagstullsbacken 23, SE-10691 Stockholm, Sweden*

Accepted 2010 December 9. Received 2010 November 9; in original form 2010 April 14

ABSTRACT

Numerical simulations of the magnetorotational instability (MRI) with zero initial net flux in a non-stratified isothermal cubic domain are used to demonstrate the importance of magnetic boundary conditions. In fully periodic systems the level of turbulence generated by the MRI strongly decreases as the magnetic Prandtl number (P_m), which is the ratio of kinematic viscosity and magnetic diffusion, is decreased. No MRI or dynamo action below $P_m = 1$ is found, agreeing with earlier investigations. Using vertical field conditions, which allow the generation of a net toroidal flux and magnetic helicity fluxes out of the system, the MRI is found to be excited in the range $0.1 \leq P_m \leq 10$, and that the saturation level is independent of P_m . In the vertical field runs strong mean-field dynamo develops and helps to sustain the MRI.

Key words: magnetic fields — MHD — turbulence — accretion, accretion discs

1 INTRODUCTION

The realization of the astrophysical significance of the magnetorotational instability (Balbus & Hawley 1991), first discovered in the context of Couette flow (Velikhov 1959; Chandrasekhar 1960), seemed to resolve the long-standing problem of the mechanism driving turbulence in accretion disks. Early numerical simulations produced sustained turbulence, large-scale magnetic fields and outward angular momentum transport (e.g. Brandenburg et al. 1995; Hawley et al. 1995). These results also showed that a significant qualitative difference exists between models where an imposed uniform magnetic field is present as opposed to the situations where such field is absent: the saturation level of turbulence and angular momentum transport are substantially higher when a non-zero vertical net flux is present (e.g. Brandenburg et al. 1995; Stone et al. 1996). Also the presence of an imposed net toroidal field seemed to enhance the transport (Stone et al. 1996).

In the meantime, a lot of numerical work has been done with zero net flux setups that omit stratification and adopt fully periodic or perfectly conducting boundaries in order to study the saturation behaviour of the MRI in the simplest possible setting (e.g. Fromang & Papaloizou 2007; Fromang et al. 2007; Liljeström et al. 2009; Korpi et al. 2010). Due to the boundary conditions, the initial net flux is conserved and no magnetic helicity fluxes out of the system are allowed. The results of these investigations have shown that as the numerical resolution of the simulations increases, or equivalently as the explicit diffusion decreases, the level of turbulence and angular momentum transport decrease, constituting a convergence problem for zero net flux MRI (Fromang et al. 2007). Runs with explicit diffusion show that sustaining turbulence becomes increasingly difficult as the magnetic

Prandtl number, $P_m = \nu/\eta$, where ν is the viscosity and η the magnetic diffusivity, is decreased (Fromang et al. 2007). Currently the convergence problem is without a definite solution. It has been suggested that this issue could be related to the P_m -dependence of the fluctuation dynamo (e.g. Schekochihin et al. 2007). It has even been argued that the MRI in periodic zero net flux systems would vanish in the limit of large Reynolds numbers and that a large-scale dynamo would be needed to sustain the MRI and turbulence (Vishniac 2009). Notably, large-scale dynamos have no problems operating at low magnetic Prandtl numbers as long as the relevant Reynolds and dynamo numbers exceed critical values (Brandenburg 2009).

From the point of view of mean-field dynamo theory (Brandenburg & Subramanian 2005), systems with fully periodic or perfectly conducting boundaries are rather special. In such closed setups magnetic helicity, defined as a volume integral of $\mathbf{A} \cdot \mathbf{B}$, where \mathbf{A} is the vector potential and $\mathbf{B} = \nabla \times \mathbf{A}$ is the magnetic field, is a conserved quantity in ideal MHD. In the presence of magnetic diffusion, magnetic helicity can change only on a timescale based on microscopic diffusivity, which is usually a very long in any astrophysical setting. Such a behaviour, which has been captured in numerical simulations (Brandenburg 2001), is well described by simple mean-field models taking into account magnetic helicity conservation (e.g. Blackman & Brandenburg 2002). This would mean that generating appreciable large-scale magnetic fields, which are possibly vital for sustaining the MRI, can take a very long time. Furthermore, the saturation value of the mean magnetic field decreases inversely proportional to the magnetic Reynolds number (e.g. Cattaneo & Hughes 1996; Brandenburg 2001). In dynamo theory this detrimental effect to

the large-scale dynamo is known as the catastrophic quenching (Vainshtein & Cattaneo 1992).

The situation, however, changes dramatically if magnetic helicity flux out of the system is allowed. In particular, the Vishniac & Cho (2001) flux, which requires large-scale velocity shear to be present and flows along the isocontours of shear, is a potential mechanism that can drive a magnetic helicity flux out of the system and alleviate catastrophic quenching. Indirect evidence for its importance exists from convection simulations in a shearing box setup (Käpylä et al. 2008, 2010b), where dynamo excitation is easier in systems with boundaries that allow a net magnetic helicity flux. However, these results can be explained by a somewhat higher critical dynamo number in the perfect conductor case (Käpylä et al. 2010b), which is a purely kinematic effect. More dramatic differences between different boundary conditions are seen in the non-linear saturation regime, with strong quenching of large-scale magnetic fields in the perfect conductor case (Käpylä et al. 2010b). The reason for this behaviour is not yet clear, especially in light of recent results of Hubbard & Brandenburg (2010) who failed to find evidence of the Vishniac–Cho flux in a numerical setup similar to ours.

In the present paper we demonstrate that the boundary conditions play a crucial role for the excitation of the MRI and the associated large-scale dynamo. Following previous work that has shown that open boundary conditions allow more efficient dynamo action (Käpylä et al. 2008, 2010b), we model a system that is isothermal, non-stratified, and the magnetic field has a zero net flux initially. We then apply vertical field boundary conditions which allow a magnetic helicity flux through the vertical boundaries by letting the magnetic field cross them. We show that if the MRI is excited, a large-scale dynamo is also excited and that the saturation level of the turbulence, large-scale magnetic field, and angular momentum transport are essentially independent of Pm. This is contrasted by periodic simulations where we find a strong Pm-dependence in accordance with earlier studies. Our results also suggest that for a given Pm the results (level of turbulence and angular momentum transport) are independent of the magnetic Reynolds number (see also Fromang 2010).

The remainder of the paper is organised as follows: in Sect. 2 we describe our model, and in Sect. 3 and 4, we present our results and conclusions.

2 THE MODEL

In an effort to keep the system as simple as possible, we assume that the fluid is non-stratified and isothermal. The diffusion processes are modeled with explicit Laplacian diffusion operators with constant coefficients. A similar model was used by Liljeström et al. (2009) and Korpi et al. (2010), although in these models higher order hyperdiffusive operators were used instead of the Laplacian ones. The computational domain is a cube with volume $H^3 = (2\pi)^3$. We solve the usual set of hydromagnetic equations in this geometry

$$\frac{\mathcal{D}\mathbf{A}}{\mathcal{D}t} = -SA_y\hat{x} - (\nabla\mathbf{U})^\top\mathbf{A} - \eta\mu_0\mathbf{J}, \quad (1)$$

$$\frac{\mathcal{D}\ln\rho}{\mathcal{D}t} = -\nabla\cdot\mathbf{U}, \quad (2)$$

$$\begin{aligned} \frac{\mathcal{D}\mathbf{U}}{\mathcal{D}t} = & -S\mathbf{U}_x\hat{y} - c_s^2\nabla\ln\rho - 2\boldsymbol{\Omega}\times\mathbf{U} \\ & + \frac{1}{\rho}(\mathbf{J}\times\mathbf{B} + \nabla\cdot 2\nu\rho\mathbf{S}), \end{aligned} \quad (3)$$

where $\mathcal{D}/\mathcal{D}t = \partial/\partial t + (\mathbf{U} + \overline{\mathbf{U}}^{(0)})\cdot\nabla$ is the advective time derivative, \mathbf{A} is the magnetic vector potential, $\mathbf{B} = \nabla\times\mathbf{A}$ is the magnetic field, and $\mathbf{J} = \mu_0^{-1}\nabla\times\mathbf{B}$ is the current density, μ_0 is the vacuum permeability, η and ν are the magnetic diffusivity and kinematic viscosity, respectively, ρ is the density, \mathbf{U} is the velocity, and $\boldsymbol{\Omega} = \Omega_0(0, 0, 1)$ is the rotation vector. The large-scale shear is given by $\overline{\mathbf{U}}^{(0)} = (0, Sx, 0)$, with $q = -S/\Omega_0 = 1.5$, corresponding to Keplerian rotation, in all runs. We use isothermal equation of state $p = c_s^2\rho$, characterised by a constant speed of sound, c_s . In the present models we choose the sound speed so that the Mach number remains of the order of 0.1 or smaller in order to minimize the effects of compressibility. The rate of strain tensor \mathbf{S} is given by

$$S_{ij} = \frac{1}{2}(U_{i,j} + U_{j,i}) - \frac{1}{3}\delta_{ij}\nabla\cdot\mathbf{U}, \quad (4)$$

where the commas denote spatial derivatives. The initial magnetic field can be written in terms of the vector potential as

$$\mathbf{A} = A_0\cos(k_Ax)\cos(k_Az)\hat{e}_y, \quad (5)$$

where the amplitude of the resulting magnetic field that contains x and z -components is given by $B_0 = k_A A_0$. We use $k_A/k_1 = 1$, $\Omega_0 = \frac{2}{3}\cdot 10^{-1}c_s k_1$, and $A_0 = \frac{1}{3}\cdot 10^{-1}\sqrt{\mu_0\rho_0}c_s k_1^{-1}$ in all models.

The values of k_A , Ω_0 and A_0 are selected so that both the wavenumber with the largest growth rate, $k_{\max} = \Omega_0/u_A = 2$, where $u_A = B_0/\sqrt{\mu_0\rho_0}$ is the Alfvén velocity, and the largest unstable wavenumber, $k_{\text{crit}} = \sqrt{2q}k_{\max} \approx 3.5$, are well resolved by the grid. The other condition for the onset of MRI, namely $\beta > 1$, where $\beta = 2\mu_0 p/B_0^2$ is the ratio of thermal to magnetic pressure, is also satisfied as $\beta = 1800$ for the maximum values of the initial magnetic field.

We use the PENCIL CODE¹ which is a high-order explicit finite difference method for solving the equations of compressible magnetohydrodynamics. Resolutions of up to 512^3 are used, see Figure 1 for a snapshot of a high resolution run.

2.1 Boundary conditions

In all models the y -direction is periodic and shearing-periodic boundary conditions are used for the x -direction (Wisdom & Tremaine 1988). On the z -boundaries we use two sets of conditions. Firstly, we apply periodic boundaries (denoted as PER).

Secondly, we apply a vertical field (VF) condition for the magnetic field, which is fulfilled when

$$B_x = B_y = B_{z,z} = 0, \quad (6)$$

at the z -boundaries. In this case we use impenetrable, stress-free conditions for the velocity according to

$$U_{x,z} = U_{y,z} = U_z = 0. \quad (7)$$

The novel property of the VF conditions is that they allow a net toroidal flux to develop and allow magnetic helicity fluxes out of the domain.

2.2 Units, nondimensional quantities, and parameters

Dimensionless quantities are obtained by setting

$$k_1 = c_s = \rho_0 = \mu_0 = 1, \quad (8)$$

¹ <http://pencil-code.googlecode.com>

Table 1. Summary of the runs. The Mach number (Ma) is given by equation (14), $\tilde{B}_{\text{rms}} = B_{\text{rms}}/B_{\text{eq}}$, and $\tilde{B}_i = \sqrt{\tilde{B}_i^2}/B_{\text{eq}}$, where B_{eq} is defined via equation (13). $\tilde{R}_{xy} = R_{xy}/(\Omega_0 H)^2$ and $\tilde{M}_{xy} = (\rho_0 \mu_0)^{-1} M_{xy}/(\Omega_0 H)^2$, where R_{xy} and M_{xy} are computed from equations (17) and (18), respectively. Finally, α_{SS} is given by equation (16).

Run	grid	Cm	Rm	Pm	Ma	\tilde{B}_{rms}	\tilde{B}_x	\tilde{B}_y	$\tilde{R}_{xy}[10^{-3}]$	$\tilde{M}_{xy}[10^{-3}]$	$\alpha_{\text{SS}}[10^{-3}]$	BC
A0	128 ³	5 · 10 ³	–	5	–	–	–	–	–	–	–	PER
A1	128 ³	10 ⁴	208	5	0.021	2.09	0.09	0.51	0.315	–2.162	2.477 ± 0.270	PER
A2	128 ³	1.5 · 10 ⁴	326	5	0.022	2.04	0.08	0.54	0.378	–2.337	2.715 ± 0.208	PER
A3	256 ³	3 · 10 ⁴	706	5	0.024	1.92	0.07	0.35	0.389	–2.564	2.953 ± 0.338	PER
A4	256 ³	3 · 10 ⁴	377	2	0.013	1.78	0.04	0.31	0.102	–0.626	0.728 ± 0.212	PER
A5	256 ³	6 · 10 ⁴	625	2	0.010	1.83	0.04	0.33	0.079	–0.441	0.520 ± 0.074	PER
A6	256 ³	3 · 10 ⁴	211	1	0.007	1.28	0.02	0.34	0.011	–0.075	0.086 ± 0.022	PER
A7	256 ³	6 · 10 ⁴	348	1	0.006	1.57	0.02	0.31	0.015	–0.088	0.103 ± 0.014	PER
B0	128 ³	1.5 · 10 ⁴	–	20	–	–	–	–	–	–	–	VF
B1	128 ³	1.5 · 10 ⁴	557	10	0.037	2.76	0.12	2.30	0.866	–4.726	5.592 ± 0.325	VF
B2	128 ³	1.5 · 10 ⁴	530	5	0.035	2.06	0.12	1.18	0.899	–4.802	5.702 ± 0.299	VF
B3	128 ³	1.5 · 10 ⁴	632	2	0.042	2.33	0.12	1.91	1.140	–4.577	5.717 ± 0.071	VF
B4	128 ³	6.0 · 10 ³	307	1	0.051	1.95	0.13	1.54	1.519	–5.463	6.982 ± 0.909	VF
B5	128 ³	1.5 · 10 ⁴	637	1	0.042	2.24	0.12	1.82	1.164	–4.422	5.586 ± 0.526	VF
B6	256 ³	3.0 · 10 ⁴	1242	1	0.041	1.77	0.11	0.97	1.018	–5.094	6.111 ± 0.560	VF
B7	256 ³	1.5 · 10 ⁴	687	0.5	0.046	1.69	0.12	1.04	1.154	–4.988	6.142 ± 0.636	VF
B8	512 ³	1.5 · 10 ⁴	719	0.2	0.048	1.55	0.11	0.87	1.111	–5.076	6.187 ± 1.068	VF
B9	512 ³	1.5 · 10 ⁴	897	0.1	0.060	1.78	0.12	1.39	1.680	–6.148	7.828 ± 1.335	VF

where ρ_0 is the mean density. The units of length, time, velocity, density, and magnetic field are then

$$\begin{aligned} [x] &= k_1^{-1}, \quad [t] = (c_s k_1)^{-1}, \quad [U] = c_s, \\ [\rho] &= \rho_0, \quad [B] = \sqrt{\mu_0 \rho_0 c_s^2}. \end{aligned} \quad (9)$$

The simulations are controlled by the following dimensionless parameters: the magnetic diffusion in comparison to viscosity is measured by the magnetic Prandtl number

$$\text{Pm} = \frac{\nu}{\eta}. \quad (10)$$

The effects of viscosity and magnetic diffusion are quantified respectively by the parameters

$$\text{Cm} = \frac{c_s}{\eta k_1^2}, \quad \frac{\text{Cm}}{\text{Pm}} = \frac{c_s}{\nu k_1^2}. \quad (11)$$

We also define the fluid and magnetic Reynolds numbers

$$\text{Re} = \frac{u_{\text{rms}}}{\nu k_1}, \quad \text{Rm} = \frac{u_{\text{rms}}}{\eta k_1} = \text{Pm Re}, \quad (12)$$

where u_{rms} is the root-mean-square (rms) value of the velocity, better describing the nonlinear outcome of the simulations. Furthermore, we often measure the magnetic field in terms of the equipartition field which is defined via

$$B_{\text{eq}} = \sqrt{\mu_0 \langle \rho u_{\text{rms}}^2 \rangle}, \quad (13)$$

where the brackets denote volume averaging. A convenient measure of the turbulent velocity is the Mach number

$$\text{Ma} = \frac{u_{\text{rms}}}{c_s}. \quad (14)$$

We define the mean quantities as horizontal averages

$$\bar{F}_i(z, t) = \frac{1}{L_x L_y} \int_{-L_x/2}^{L_x/2} \int_{-L_y/2}^{L_y/2} F_i(x, y, z, t) dx dy. \quad (15)$$

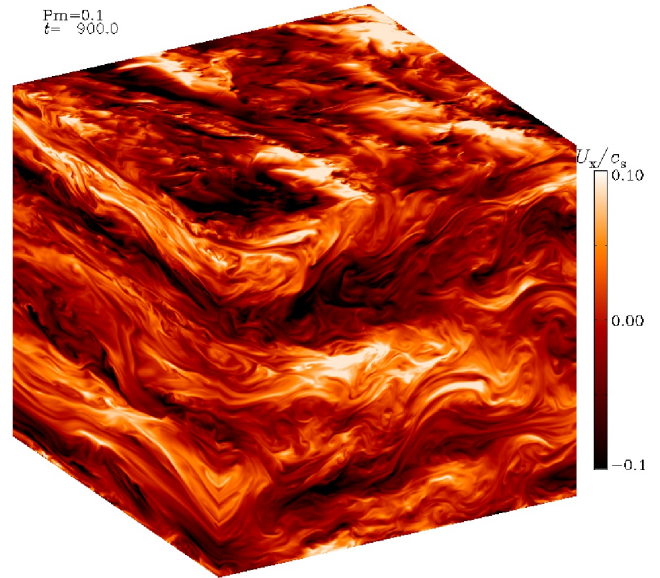


Figure 1. Velocity component U_x from the periphery of the domain for Run B9 with $\text{Pm} = 0.1$, $\text{Cm} = 1.5 \cdot 10^4$, and $\text{Re} \approx 9 \cdot 10^3$. See also <http://www.helsinki.fi/~kapylla/movies.html> for animations.

Often an additional time average over the statically saturated state is also taken. The size of error bars is estimated by dividing the time series into three equally long parts. The largest deviation of the average for each of the three parts from that over the full time series is taken to represent the error.

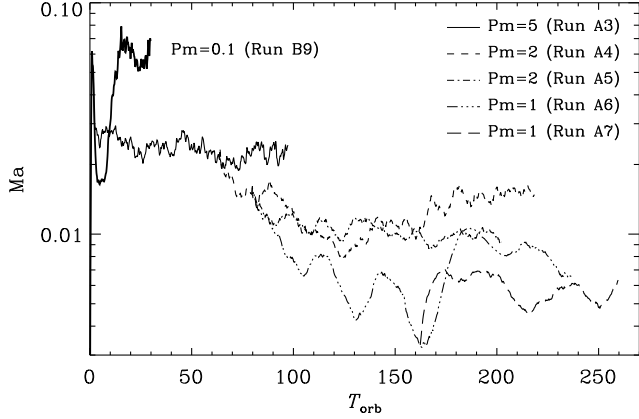


Figure 2. Mach number defined via equation (14) for Runs A3–A7. The thick solid line shows the Mach number for Run B9 with $Pm = 0.1$ and VF boundaries.

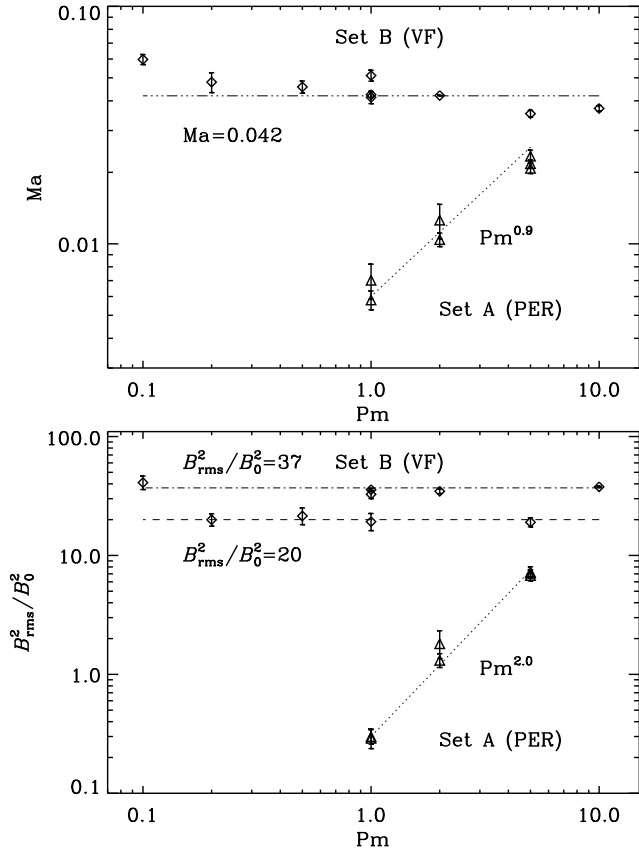


Figure 3. Mach number (upper panel) and magnetic energy (lower panel) as functions of magnetic Prandtl number for periodic (triangles) and vertical field (diamonds) boundary conditions. The magnetic field is normalised by the rms value of the initial field.

3 RESULTS

We perform two sets of simulations listed in Table 1 where we use either periodic (Set A) or vertical field (Set B) boundary conditions. In Set A, Runs A0–A3 were started with the initial conditions described in Section 2 whereas Runs A4–A6 were continued from a snapshot of Run A3 in the saturated state, see Fig. 2. Run A7 was

continued from a snapshot of Run A6 with a two times lower diffusivities at roughly $150T_{\text{orb}}$ where $T_{\text{orb}} = 2\pi/\Omega_0$ is the orbital period. The minimum duration of the runs in Set A is $100T_{\text{orb}}$. Runs in Set B were all started from scratch and typically ran a significantly shorter time than those in Set A, e.g. $\sim 30T_{\text{orb}}$ in the low- Pm cases (see Fig. 2), because final saturation occurs much faster.

3.1 Saturation level of the MRI

3.1.1 Periodic case

Earlier studies have shown that exciting the MRI in a periodic zero net flux system becomes increasingly harder as the magnetic Prandtl number is decreased (Fromang et al. 2007). Furthermore, the saturation level of turbulence has been reported to decrease as a function of Pm . This has been conjectured to be associated with the difficulties of exciting a small-scale or fluctuation dynamo at low Pm (e.g. Schekochihin et al. 2007). It is, however, unclear how the saturation level of the small-scale dynamo is affected by this. It is conceivable that at magnetic Reynolds numbers close to marginal it takes a long time to reach saturation and that the current simulations have not been run long enough. On the other hand, if catastrophic quenching is to blame, the *mean* magnetic field should decrease as Rm^{-1} (e.g. Brandenburg & Subramanian 2005, and references therein). A further possibility is the scenario suggested by Vishniac (2009): in the absence of an outer scale for the magnetic field, the microscopic diffusivities determine the minimum length scale of MRI, which leads to turbulence intensity decreasing proportional to $Rm^{-2/3}$.

We study this issue by performing runs keeping Pm fixed and increasing the Reynolds numbers. We find that the saturation level of turbulence, measured by the Mach number and root mean square value of magnetic field, are unaffected when Cm is increased by a factor of three for the case $Pm = 5$ (Runs A1–A3) and by a factor of two for the cases $Pm = 2$ (Runs A4–A5) and $Pm = 1$ (Runs A6–A7), see Table 1 and Fig. 3. Furthermore, the Mach number and rms magnetic field, normalised with the rms value of the initial field, increase roughly linearly with Pm . The Pm -dependence of rms magnetic field normalised to the equipartition field strength, listed in Table 1, shows a much weaker trend. This is to be expected as B_{eq} is proportional to the rms velocity which, on the other hand, is a produced by the magnetic field itself. Since the parameter range of our simulations is rather limited, no definite conclusions can be drawn. However, taking the results at face value, it appears that Pm , not Cm , is the parameter that determines the saturation level in the periodic zero net flux case. Recently, Fromang (2010) reached the same conclusion independently for the case of $Pm = 4$. According to our results, the catastrophic quenching and the diffusivity-limited MRI length scale scenarios would be ruled out. Although there is the possibility that our calculations have not been run long enough, the results seem to suggest the small-scale dynamo being harder to excite as Pm decreases.

3.1.2 Vertical field case

We find that the saturation behaviour is markedly different when vertical field boundary conditions are applied (Table 1 and Fig. 3). The saturation level of turbulence depends only weakly on the magnetic Prandtl number: the difference of the values of u_{rms} between $Pm = 0.1$ and $Pm = 10$ cases is roughly 50 per cent. Furthermore, the Mach number decreases as function of Pm , the trend be-

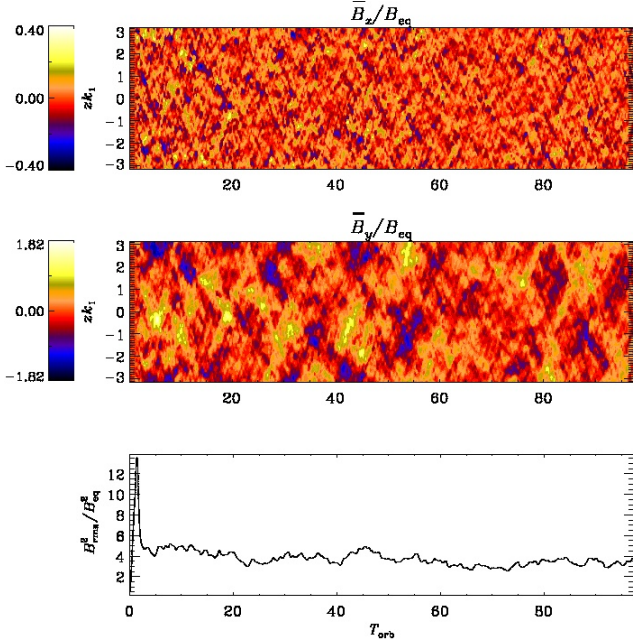


Figure 4. Horizontally averaged horizontal magnetic fields \overline{B}_x (top panel) and \overline{B}_y (middle) for Run A3 with $C_m = 3 \cdot 10^4$ and $P_m = 5$. The lower panel shows the square of the rms-value of the total magnetic field.

ing weaker but opposite to the periodic case. This is likely caused by the increase of viscosity by two orders of magnitude rather than the intrinsic dependence of the MRI on P_m . This conjecture is supported by the saturation values of the magnetic fields which are independent of P_m (lower panel of Fig. 3). The runs in Set B, however, seem to fall into two distinct regimes of magnetic field strength, where the magnetic energy differs by roughly a factor of two. The reason for this apparent discrepancy is that a different mode of the large-scale magnetic field is excited in the different branches (see below). Similar behaviour of the large-scale dynamo has previously been seen in isotropically forced turbulence (Brandenburg & Dobler 2002).

3.2 Large-scale magnetic fields

In the runs with periodic boundaries we occasionally see the emergence of large-scale magnetic fields with a sinusoidal dependence on z (see Fig. 4), i.e. $k/k_1 = 1$, in accordance with earlier investigations (Lesur & Ogilvie 2008). Similar large-scale dynamos have recently been reported from nonhelically forced turbulence with shear where the MRI is absent (e.g. Yousef et al. 2008; Brandenburg et al. 2008). As in the forced turbulence case a strong large-scale field is not present at all times and the fields undergo apparently random sign changes that are not fully understood (see, however, Lesur & Ogilvie 2008; Brandenburg et al. 2008). The intermittent nature of the large-scale fields could also explain the apparent lack of catastrophic quenching of the time averaged mean magnetic field (see Table 1).

In the vertical field runs a strong large-scale dynamo is always excited continuously. The two branches of solutions that are visible in the total magnetic energy (Fig. 3) are due to different modes of the large-scale field. This is illustrated in Fig. 5 where the horizontally averaged horizontal magnetic field components are shown as functions of time for Run B1. As is common for dynamos

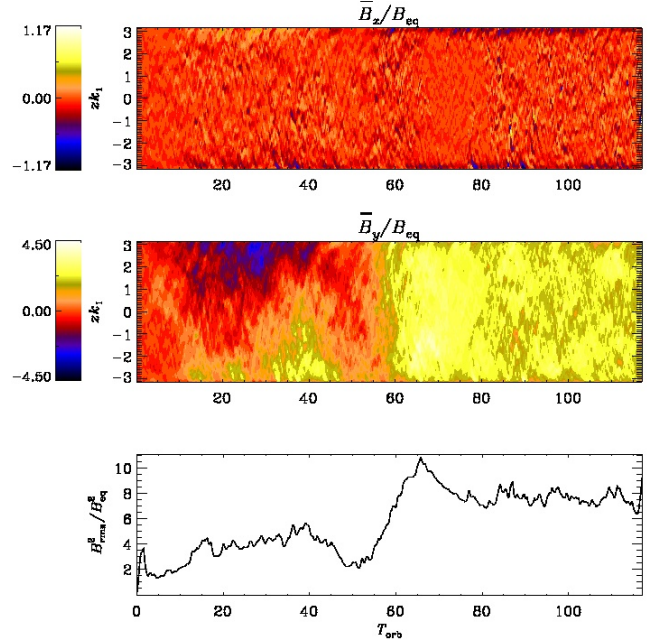


Figure 5. Same as Fig. 4 but for Run B1 with $C_m = 1.5 \cdot 10^4$ and $P_m = 10$.

with strong shear, the streamwise component of the magnetic field is much stronger than the cross-stream one. Although the initial condition of the magnetic field is the same in all runs, the large-scale field which develops in the non-linear stage can choose any of the available wavenumbers consistent with the vertical boundary condition $B_x = B_y = 0$. In practice, the dominant large-scale component is $k/k_1 = 1$ or $k/k_1 = \frac{1}{2}$ in our simulations. The large-scale dynamo tends to accumulate energy at the smallest possible wavenumber (Brandenburg 2001), i.e. the largest spatial scale. However, if the dominant mode is on some intermediate scale initially, those modes can also be long-lived (Brandenburg & Dobler 2002). Ultimately the large-scale field evolves towards final saturation where the largest possible scale dominates which was seen in Brandenburg & Dobler (2002) and in some of our runs (cf. Fig. 5). The fact that the magnetic energy in Runs B2, B6, B7, and B8 is smaller is due to the fact that the large-scale field is predominantly of the $k/k_1 = 1$ flavour, and that final saturation of the large-scale magnetic field has not yet occurred. Lesur & Ogilvie (2008) found that the toroidal large-scale magnetic field generated in their simulations is close to that yielding the maximum growth rate for an $m = 1$ non-axisymmetric instability. Using their notation we find a similar result so that $\overline{B}_y k_y / (-S \sqrt{5/12} \sqrt{\mu_0 \rho}) \approx 0.6$ for $k/k_1 = 1$ and 1.2 for $k/k_1 = \frac{1}{2}$, using $k_y/k_1 = 1$ for the $m = 1$ mode. However, the full significance of this result is as of yet unclear.

Although the source of the turbulence and the nature of the dynamos (kinematic vs. nonlinear) is different between the non-helically forced turbulence simulations (e.g. Yousef et al. 2008; Brandenburg et al. 2008) and the non-stratified MRI runs such as those presented here, it is conceivable that the large-scale field generation mechanism is the same. Since the periodic system is homogeneous, the cause of the large-scale fields cannot be the α -effect of mean-field dynamo theory (Moffatt 1978; Krause & Rädler 1980), which is in simple systems proportional to the density gradient or the turbulence inhomogeneity due to boundaries (e.g.

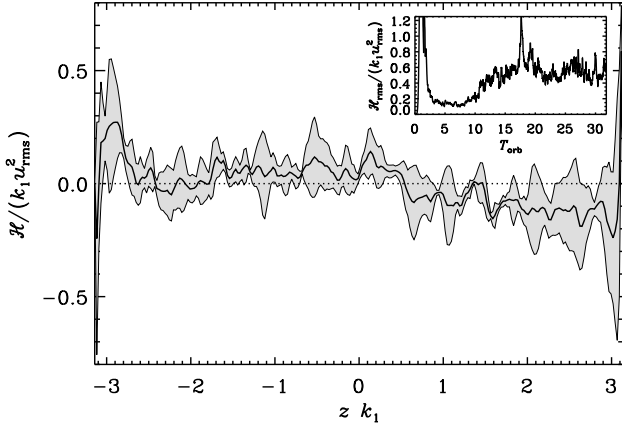


Figure 6. Horizontally averaged kinetic helicity \mathcal{H} from Run B7. The inset shows the volume averaged rms-value of \mathcal{H} . The shaded area denotes the error estimates.

Giesecke et al. 2005; Käpylä et al. 2010a). However, a fluctuating α with zero mean can also drive a large-scale dynamo when shear is present (e.g. Vishniac & Brandenburg 1997; Sokolov 1997; Silant’ev 2000; Proctor 2007). This is the most likely source of the large-scale magnetic fields in the present case. Furthermore, it is possible that the shear–current and $\boldsymbol{\Omega} \times \boldsymbol{J}$ -effects can drive a large-scale dynamo (Rädler 1969; Rogachevskii & Kleeorin 2003, 2004), although present evidence from numerical models does not support this (Brandenburg et al. 2008).

In the VF runs the impenetrable stress-free z -boundaries make the turbulence inhomogeneous near the boundary. This leads to the generation of mean kinetic helicity $\mathcal{H}(z) = \overline{\boldsymbol{\omega} \cdot \boldsymbol{u}}$, where $\boldsymbol{\omega} = \nabla \times \boldsymbol{u}$ is the vorticity. The quantity \mathcal{H} is important, because the mean-field α -effect is, in simple settings, proportional to it (e.g. Krause & Rädler 1980). Such contributions, however, will not show up in volume averages because the sign of the helicity, and thus of the α -effect, are different near the different boundaries. Figure 6 shows the horizontally averaged kinetic helicity for Run B7. Here we average also in time over the saturated state of the run. In most of the volume the kinetic helicity is consistent with zero, although there are regions close to the boundaries where non-zero mean values are present. The rms-value of \mathcal{H} , however, is at least five times greater than its mean (see the inset of Fig. 6). Note also that the normalization factor contains the integral scale k_1 . A more proper definition would be to use the wavenumber where turbulent energy peaks which is likely at least a factor of few greater than k_1 . Thus our estimates for the normalised helicity can be considered as upper limits. The rather small values of mean helicity and the dominance of fluctuations suggest that the generation mechanism of the large-scale fields could indeed be the incoherent α -shear dynamo. However, a conclusive answer can only be obtained by extracting the turbulent transport coefficients and by performing mean-field modeling of the same system (see e.g. Gressel 2010).

3.3 Angular momentum transport

The main effect of turbulence in astrophysical disks is to enhance diffusion which enables efficient accretion. In accretion disk theory it is customary to parametrise the turbulent viscosity ν_t in terms of the Shakura–Sunyaev viscosity parameter α_{SS} , which relates ν_t with the local gas pressure (Shakura & Sunyaev 1973).

We define the Shakura–Sunyaev viscosity parameter as

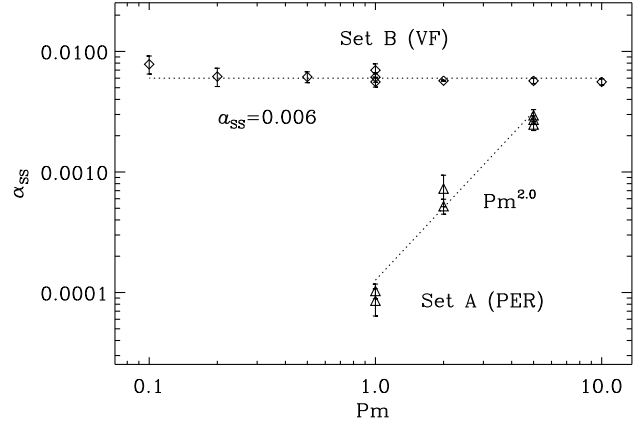


Figure 7. Viscosity parameter α_{SS} as a function of Pm for the runs listed in Table 1. The dotted lines show $\alpha_{SS} = \text{const} = 6 \cdot 10^{-3}$ and $\alpha_{SS} \propto \text{Pm}^{2.0}$ for reference.

(Brandenburg et al. 2004)

$$\alpha_{SS} = \frac{[R_{xy} - M_{xy}/(\mu_0\rho)]}{(\Omega_0 H)^2}, \quad (16)$$

where

$$R_{xy} \equiv \langle u_x u_y \rangle = \langle U_x U_y \rangle - \langle \overline{U}_x \overline{U}_y \rangle, \quad (17)$$

is the Reynolds stress and

$$M_{xy} \equiv \langle b_x b_y \rangle = \langle B_x B_y \rangle - \langle \overline{B}_x \overline{B}_y \rangle, \quad (18)$$

the Maxwell stress, and where the angular brackets denote volume averaging. Here we decompose the velocity and magnetic field into their mean (\overline{U} , \overline{B}), taken here as the horizontal average, and fluctuating (u , b) parts. The mean velocities show no systematic large-scale pattern and the remaining signal $\overline{U} \sim \mathcal{O}(0.05 u_{\text{rms}})$ is likely a residual of averaging over a finite number of cells. The contribution of mean flows to the angular momentum transport and the dynamo process is thus likely to be negligible.

For the runs in Set A we find essentially the same scaling, consistent with $\text{Pm}^{2.0}$, with magnetic Prandtl number as in the case of the turbulent kinetic and magnetic energies, see Fig. 7. This is consistent with the mixing length estimate of turbulent viscosity which is proportional to the turbulence intensity (e.g. Snellman et al. 2009). The numerical values of α_{SS} decrease from $\approx 10^{-3}$ for $\text{Pm} = 5$, to $\alpha_{SS} \approx 10^{-4}$ for $\text{Pm} = 1$. In Set B, on the other hand, α_{SS} is essentially independent of magnetic Prandtl number. The value of α_{SS} is consistently of the order of $6 \cdot 10^{-3}$, which is significantly greater than that found in runs with periodic boundaries. Here the qualitative behaviour of α_{SS} resembles that of the turbulent kinetic energy, whereas the two different dynamo modes seen in magnetic energy are not visible in the angular momentum transport.

3.4 Discussion

A possible clue to understanding the convergence problem in zero net flux simulations comes from MRI models with density stratification: in them the level of turbulence does converge when the Reynolds numbers are increased (Davis et al. 2010), even with perfect conductor of periodic boundaries. Furthermore, such setups exhibit a large-scale dynamo (e.g. Brandenburg et al.

1995; Stone et al. 1996; Gressel 2010) where the magnetic helicity changes sign at the midplane (Gressel 2010).

Recent numerical results from a different setting suggest that a diffusive flux of magnetic helicity also exists (Mitra et al. 2010). Such a flux can alleviate catastrophic quenching by transporting oppositely signed magnetic helicity to the midplane where annihilation occurs. This could explain the successful convergence of the stratified MRI runs. In the non-stratified case with periodic or perfectly conducting boundaries, however, no net flux of magnetic helicity occurs and the large-scale dynamo can be catastrophically quenched, shutting off the MRI. When a flux is allowed by changing to vertical field boundary conditions, this limitation is removed and the large-scale dynamo can operate without hindrance. However, this hypothesis requires further study and more careful analysis of the helicity fluxes that we postpone to a future publication.

4 CONCLUSIONS

We present three-dimensional numerical simulations of the magnetorotational instability in an isothermal non-stratified setup with zero net flux initially. Using fully periodic boundaries, that do not allow the generation of a mean toroidal flux or magnetic helicity fluxes out of the system, we encounter the convergence problem (Fromang et al. 2007) of the MRI: turbulent kinetic and magnetic energies, and the angular momentum transport increase approximately proportional to the magnetic Prandtl number. Intermittent large-scale magnetic fields are observed in the periodic runs. Increasing the Reynolds numbers moderately at a given Pm does not appear to markedly change the results in the saturated state.

When vertical field boundary conditions, allowing the generation of a mean flux and a magnetic helicity flux, are used, the MRI is excited at least in the range $0.1 \leq Pm \leq 10$ for our standard value of $C_m = 1.5 \cdot 10^4$. We find that the saturation level of the turbulence and the angular momentum transport are only weakly dependent on the Prandtl number and that strong large-scale fields are generated in all cases. The Shakura–Sunyaev viscosity parameter has consistently a value of $\alpha_{SS} \approx 6 \cdot 10^{-3}$ in the vertical field case. Exploring even lower values of Pm is infeasible at the moment due to prohibitive computational requirements but there are no compelling arguments against a large-scale dynamo operating at low Pm (Brandenburg 2009). We conjecture that the operation of the MRI at low Pm is due to the efficient large-scale dynamo in the system. It is conceivable that the dynamo only works if magnetic helicity is allowed to escape (see also Vishniac 2009) or annihilate at the disk midplane due to an internal diffusive flux (Mitra et al. 2010). However, measuring the magnetic helicity fluxes in the presence of boundaries is difficult due to the fact that they are in general gauge dependent (e.g. Brandenburg et al. 2002; Hubbard & Brandenburg 2010).

The current results highlight the close connection between dynamo theory and the theory of magnetised accretion disks (see also Blackman 2010) and the importance of studying the results in a common framework (e.g. Gressel 2010). Clearly, a more thorough study is needed in order to substantiate the possible role of magnetic helicity fluxes for the excitation and saturation of the MRI. We plan to address these issues in future publications.

ACKNOWLEDGMENTS

The authors acknowledge Axel Brandenburg for his helpful comments on the manuscript. The numerical simulations were performed with the supercomputers hosted by CSC – IT Center for Science in Espoo, Finland, who are administered by the Finnish Ministry of Education. Financial support from the Academy of Finland grant Nos. 121431 (PJK) and 112020 (MJK), are acknowledged. The authors acknowledge the hospitality of NORDITA during the program “Solar and Stellar Dynamos and Cycles”.

REFERENCES

- Balbus, S. A., Hawley, J.F. 1991, *ApJ*, 376, 214
 Blackman, E.G., & Brandenburg, A. 2002, *ApJ*, 579, 359
 Blackman, E. 2010, *Astron. Nachr.*, 331, 101
 Brandenburg, A., Nordlund, Å., Stein, R. F., & Torkelsson, U. 1995, *ApJ*, 446, 741
 Brandenburg, A. 2001, *ApJ*, 550, 824
 Brandenburg, A. & Dobler, W. 2002, *Comp. Phys. Comm.*, 147, 471
 Brandenburg, A., Dobler, W., Subramanian, K. 2002, *Astron. Nachr.*, 323, 99
 Brandenburg, A., Dintrans, B., & Haugen, N.E.L. 2004, *AIPC*, 733, 122
 Brandenburg, A. & Subramanian, K. 2005, *Phys. Rep.*, 417, 1
 Brandenburg, A., Rädler, K.-H., Rheinhardt, M. & Käpylä, P.J. 2008, *ApJ*, 676, 740
 Brandenburg, A. 2009, *ApJ*, 697, 1206
 Cattaneo, F. & Hughes, D. W. 1996, *Phys. Rev. E*, 54, 4532
 Chandrasekhar, S. 1960, *Proc. Nat. Acad. Sci.*, 46, 253
 Davis, S. W., Stone, J. M., Pessah, M. E. 2010, *ApJ*, 713, 52
 Fromang, S. & Papaloizou, J. 2007, *A&A*, 476, 1113
 Fromang, S., Papaloizou, J., Lesur, G. & Heinemann, T. 2007, *A&A*, 476, 1123
 Fromang, S. 2010, *A&A*, 514, L5
 Giesecke, A., Ziegler, U. & Rüdiger, G. 2005, *Phys. Earth Planet. Int.*, 152, 90
 Gressel, O., 2010, *MNRAS*, 405, 41
 Hawley, J.F., Gammie, C. F. & Balbus, S. A. 1995, *ApJ*, 440, 742
 Hubbard, A., Brandenburg, A., 2011, *ApJ*, 727, 11
 Korpi, M. J., Käpylä, P. J., Väisälä, M. S. 2010, *Astron. Nachr.*, 331, 34
 Käpylä, P. J., Korpi, M. J. & Brandenburg, A. 2008, *A&A*, 491, 353
 Käpylä, P. J., Korpi, M. J. & Brandenburg, A. 2010a, *MNRAS*, 402, 1458
 Käpylä, P. J., Korpi, M. J. & Brandenburg, A. 2010b, *A&A*, 518, A22
 Krause F., Rädler K.-H. 1980, *Mean-field magnetohydrodynamics and dynamo theory* (Pergamon Press, Oxford)
 Lesur, G. & Ogilvie, G. 2008, *A&A*, 488, 451
 Liljeström, A. J., Korpi, M. J., Käpylä, P. J., Brandenburg, A., Lyra, W. 2009, *Astron. Nachr.*, 330, 91
 Mitra, D., Candelaresi, S., Chatterjee, P., Tavakol, R. & Brandenburg, A. 2010, *Astron. Nachr.*, 331, 130
 Moffatt, H. K. 1978, *Magnetic field generation in electrically conducting fluids* (Cambridge Univ. Press, Cambridge)
 Proctor M. R. E. 2007, *MNRAS*, 382, L39
 Rädler, K.-H., 1969, *Monatsber. Dtsch. Akad. Wiss. Berlin*, 11, 194

- Rogachevskii I., Kleeorin N. 2003, Phys. Rev. E, 68, 036301
Rogachevskii I., Kleeorin N. 2004, Phys. Rev. E, 70, 046310
Schekochihin, A.A., Iskakov, A. B., Cowley, S. C., McWilliams, J. C., Proctor, M. R. E. & Yousef, T. A., 2007, NJP, 9, 300
Shakura, N. I. & Sunyaev, R. A. 1973, A&A, 24, 337
Silant'ev N. A. 2000, A&A, 364, 339
Snellman, J. E., Käpylä, P. J., Korpi, M. J., & Liljeström, A. J., 2009, A&A, 505, 955
Sokolov D. D. 1997, Astron. Reports, 41, 68
Stone, J. M., Hawley, J. F., Gammie, C. F. & Balbus, S. A. 1996, ApJ, 463, 656
Vainshtein, S. I. & Cattaneo, F. 1992, ApJ, 393, 165
Velikhov, E.P. 1959, Sov. Phys. JETP, 36, 1398
Vishniac E. T., Brandenburg A. 1997, ApJ, 475, 263
Vishniac E. T., Cho J. 2001, ApJ, 550, 752
Vishniac E. T. 2009, ApJ, 696, 1021
Wisdom, J., Tremaine, S. 1988, AJ, 95, 925
Yousef T. A., Heinemann T., Schekochihin A. A., Kleeorin N., Rogachevskii I., Iskakov A. B., Cowley S. C., McWilliams J. C. 2008, Phys. Rev. Lett., 100, 184501